International Tables for Crystallography (2012). Vol. F, Chapter 9.3, pp. 234–239.

Chapter 9.3. X-ray diffraction imaging of whole cells

D. Shapiro

9.3.1. Introduction

The brightness of third-generation synchrotron X-ray sources removes the need to enhance a diffracted X-ray signal with crystallographic redundancy for certain classes of samples. This is particularly useful for samples for which there exists only one unique structure or for which arrangement into a crystalline form is exceedingly difficult. Single-particle X-ray diffraction microscopy, also known as coherent X-ray diffraction microscopy (CXDM), treats an isolated non-crystalline sample as a crystallographer treats a crystal. The far-field diffraction intensity pattern of the sample is measured and the phase problem is solved computationally, allowing for structure recovery through a Fourier transform. Since Mother Nature restricts us to only measuring intensities, all methods of phase retrieval rely on decoding phase information that has been encoded in intensity measurements. Crystallographers, and the subsequent diffraction microscopists, have two basic methods for doing this. The first, the holographic method, mixes a known reference signal with the desired and unknown signal. The coherent superposition of these two signals results in measureable intensity variations that are directly related to the relative phase. This is, indirectly, a phase-measuring method. The second method relies only on the signal from the unknown structure and additional information, supplied by the scientist, which is physically plausible. This is a constraint-based method. Both methods seek to fill the information deficit inherent in intensity measurements by adding something that may unlock the phase.

In 1980, David Sayre suggested that CXDM should be possible (Sayre, 1980). Algorithms being developed for electron microscopy in the early 1970s would establish the constraint-based paradigm of iterative phase retrieval from Fourier modulus measurements. In particular, the alternating projection algorithm of Gerchberg and Saxton, the error-reduction algorithm, was developed to reconstruct the phase information that is missing when intensity measurements are made in both real and reciprocal space (Gerchberg & Saxton, 1972). This algorithm was later modified by Fienup into the input–output algorithm to handle cases where only one intensity measurement is made (Fienup, 1978, 1982; Fienup *et al.*, 1982; Miao *et al.*, 1998). In this case, the required real-space constraint restricts the object to an area no larger than half the width of its autocorrelation. The combination of the input–output algorithm and the error-reduction algorithm was found to be a very robust method of image reconstruction using only Fourier domain intensities, but its success was not understood for several years. In 1982, Bates argued that the solutions to the phase problem are unique in two dimensions if the Fourier modulus is sampled on an interval at least twice as fine as the Bragg interval (Bates & Fright, 1983; Bates, 1982). The method of phase retrieval from diffraction patterns sampled between Bragg peaks became known as the oversampling phasing method (Sayre, 1991; Sayre & Chapman, 1995; Miao *et al.*, 1998). The oversampling method compensates for the information deficit by supplying a zero-density region of approximately known size in the object domain. The more finely the diffraction pattern is sampled, the larger this zero-density region is, although this only adds useful information up to a certain point. This addition of information through Fourier space sampling results in an overdetermined inverse problem with a unique solution.

Sayre considered that the real niche of CXDM would be imaging objects of a few microns at a resolution of a few nanometres using soft X-rays (1–10 nm wavelength). Indeed, since the initial demonstration of CXDM (Fig. 9.3.1.1), ten years ago at the time of writing, active research projects have developed at all major synchrotron facilities and the technique has been applied to a diverse set of scientific problems. Three-dimensional images of radiation-hard materials have been obtained at 15 nm resolution, while two-dimensional images of a whole cell at 30 nm and of a gold nanoparticle at 5 nm resolutions have been reported, among many others (Miao *et al.*, 2002; Shapiro *et al.*, 2005; Pfeifer *et al.*, 2006; Barty *et al.*, 2008; Schroer *et al.*, 2008; Nelson *et al.*, 2010). CXDM researchers have not yet achieved the 'holy grail' of cellular imaging, the imaging of a whole frozen hydrated cell in three dimensions, but at least two teams are pursuing this goal with recent success in the two-dimensional case (Huang *et al.*, 2009; Lima *et al.*, 2009). Lens-based X-ray microscopes have achieved this landmark with moderate resolution (Wang *et al.*, 2000; Weiss *et al.*, 2000; Larabell & Le Gros, 2004). Transmission X-ray microscopes (TXM) and scanning transmission X-ray microscopes (STXM) utilizing diffractive zone plate lenses have high throughput and the advantage of direct imaging, but are limited in resolution by the technological challenge of making efficient high-numerical-aperture lenses. TXM can now routinely image in three dimensions at 50 nm resolution, and 12 nm resolution has

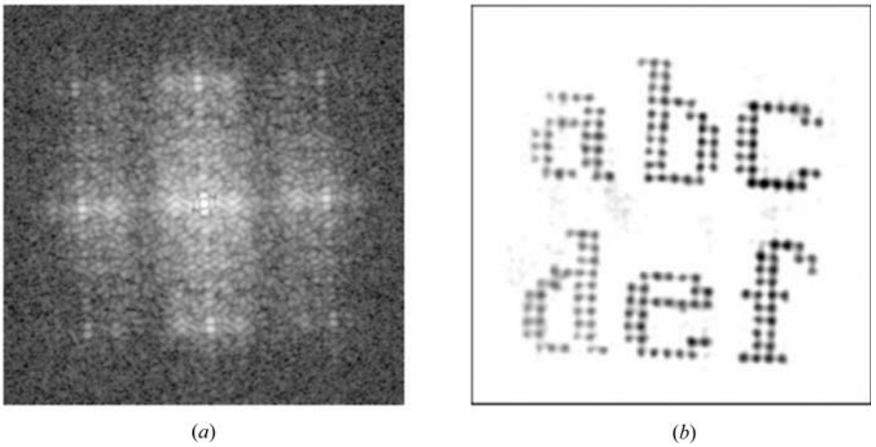

Figure 9.3.1.1
First soft X-ray demonstration of the CXDM method. (*a*) Diffraction pattern using 1.7 nm X-rays. (*b*) Reconstruction of (*a*) to 75 nm resolution. Reprinted by permission from Macmillan Publishers Ltd: *Nature* (Miao *et al.*, 1999), copyright (1999).

Table 9.3.2.1
Summary of various algorithms

The algorithms are, from top to bottom: error reduction, solvent flipping, hybrid input–output, difference map, averaged successive reflections, hybrid projection–reflection and relaxed averaged alternating reflections. A reflection is defined by its associated projection as $\mathbf{R} = 2\mathbf{P} - \mathbf{I}$, where $\mathbf{I}$ is the identity projection (Marchesini, 2007).

Algorithm	Iteration $\rho^{(n+1)} =$
ER	$\boldsymbol{P}_s\boldsymbol{P}_m\rho^{(n)}$
SF	$\boldsymbol{R}_s\boldsymbol{P}_m\rho^{(n)}$
HIO	$\begin{cases}\boldsymbol{P}_m\rho^{(n)}(\boldsymbol{r}), & \boldsymbol{r}\in S\\ (\boldsymbol{I}-\beta\boldsymbol{P}_m)\rho^{(n)}(\boldsymbol{r}), & \boldsymbol{r}\notin S\end{cases}$
DM	$\{\boldsymbol{I}+\beta\boldsymbol{P}_s[(1+\gamma_s)\boldsymbol{P}_m-\gamma_s\boldsymbol{I}]$ $-\beta\boldsymbol{P}_m[(1+\gamma_m)\boldsymbol{P}_s-\gamma_m\boldsymbol{I}]\}\rho^{(n)}$
ASR	$(1/2)[\boldsymbol{R}_s\boldsymbol{R}_m+\boldsymbol{I}]\rho^{(n)}$
HPR	$(1/2)\{\boldsymbol{R}_s[\boldsymbol{R}_m+(\beta-1)\boldsymbol{P}_m]+\boldsymbol{I}+(1-\beta)\boldsymbol{P}_m\}\rho^{(n)}$
RAAR	$[(1/2)\beta(\boldsymbol{R}_s\boldsymbol{R}_m+\boldsymbol{I})+(1-\beta)\boldsymbol{P}_m]\rho^{(n)}$

been demonstrated in two dimensions, although the total efficiency of the optic used was of the order of 1% (Chao *et al.*, 2009) at the highest spatial frequencies. Thus, at the cost of throughput and ease of use, a diffraction microscope provides increased X-ray efficiency and resolution.

The following sections first report on the current standard single-particle phase retrieval techniques and then on recent experiments in CXDM, which establish the state of the art in whole-cell imaging by diffractive methods. Images of dry yeast at 11 nm resolution are presented, which represent the highest resolution X-ray images of whole cells currently on record. The effects of radiation damage are discussed and Sayre's idea of using stereoscopic viewing as a means of obtaining quick and low-dose three-dimensional information is explored (Sayre, 2008).

9.3.2. Phase retrieval from single-particle diffraction data

The problem of phase retrieval is solved through successive application of constraints on the recovered object in the data and object spaces. Using the language of convex optimization, the mathematical operators which act on the data are projectors. The projector in the reciprocal (data) space forces the Fourier components to have the correct magnitude, while in object space finite support is enforced. To calculate the Fourier magnitude projector, one first needs to propagate the object density, ρ, to the data space by a Fourier transform, then replace the estimated magnitudes $|\tilde{\rho}|$ with the measured ones, $I^{1/2}$, and finally propagate back to real space. Using these transforms one simplifies the calculation of the projection, which becomes an element-wise operation on each recovered Fourier component. The forward $\mathcal{F}$ and inverse $\mathcal{F}^{-1}$ transforms must be incorporated into the operator defined in real space $\mathbf{P}_m$,

$$\mathbf{P}_m = \mathcal{F}^{-1}\tilde{\mathbf{P}}_m\mathcal{F}, \tag{9.3.2.1}$$

where the measured Fourier magnitudes are enforced in Fourier space by $\tilde{\mathbf{P}}_m$. Using the Fourier basis, one simply replaces the estimated magnitudes $|\tilde{\rho}|$ with the measured ones $I^{1/2}$, $[\tilde{\mathbf{P}}_m\tilde{\rho}(\boldsymbol{k}) = I(\boldsymbol{k})^{1/2}\tilde{\rho}(\boldsymbol{k})/|\tilde{\rho}(\boldsymbol{k})|]$. Similarly, in the object space the finite support constraint is applied on a per pixel basis through multiplication by the support mask. The corresponding projector is

$$\mathbf{P}_s\rho = S\cdot\rho.$$

Table 9.3.2.1 lists the combination of projections used by the most popular algorithms.

The violation of the support constraint is used as an error metric to monitor the convergence towards the solution. The solution should have zero density outside the support mask, so the error can be defined as the total density outside the support area,

$$\varepsilon_s^2(\rho) = |||\rho - S\rho|||^2 = ||[I-\mathbf{P}_s]\rho||^2. \tag{9.3.2.2}$$

Alternatively, the error metric can be defined in the data space as the difference between the measured and calculated magnitudes,

$$\varepsilon_m^2(\rho) = |||\mathcal{F}\rho| - I^{1/2}||^2 = ||[I-\mathbf{P}_m]\rho||^2. \tag{9.3.2.3}$$

In reality, the measured intensities are subject to noise which prohibits exact compliance with the constraints, so the error metrics cannot drop to zero. Although in most cases the algorithm can locate the global minimum, random noise will force fluctuations around the minimum. Once the algorithm reaches this steady-state regime, any particular iterate chosen as the solution would have a misleading degree of detail. On the other hand, the average of many fluctuating iterates would have reduced intensity in those Fourier components which are not reliably phased. The ratio of the average Fourier magnitude to the measured magnitude provides a measure of the stability, or reproducibility, of the retrieved phase information. This ratio as a function of spatial frequency is the phase retrieval transfer function (PRTF),

$$\mathrm{PRTF}(\mathbf{q}) = \frac{|\mathcal{F}[\langle\psi\rangle]|(\mathbf{q})}{[I_m(\mathbf{q})]^{1/2}}, \tag{9.3.2.4}$$

where $\mathcal{F}[\langle\psi\rangle]$ is the Fourier transform of the final averaged image and I_m is the measured intensity pattern. The PRTF is analogous to the differential phase residual of electron microscopy and, following Chapman *et al.* (2006), the resolution of a reconstruction is chosen as the spatial frequency at which the PRTF falls below a value of 0.5.

9.3.3. High-resolution imaging of yeast

The X-ray dose required to image a given volume of protein is nearly independent of energy above the oxygen K edge. At the same time, the photon flux required to image the same volume increases with E^2 because of the energy dependence of the scattering cross section (Howells *et al.*, 2009). For this reason, it is advantageous to use the lowest energy commensurate with the desired resolution of 5–10 nm. Commercially available charge-coupled device (CCD) detectors can easily provide a scattering angle of 0.1 radians [a 1 inch detector placed 5 inches from the sample (1 inch = 2.54 cm)], which results in a half-period resolution of 8 nm when using 750 eV X-rays. Furthermore, a cell with a diameter of 3 µm would have an oversampling ratio (number of intensity samples per speckle) of at least ten in this geometry if the detector has 20 µm pixels.

In this particular case, a Princeton Instruments CCD (PI-MTE:1300) is placed 136 mm downstream of a freeze-dried yeast cell using the CXDM instrument on Beamline 9.0.1 of the Advanced Light Source (ALS). The yeast cell is illuminated by a coherent beam of 750 eV X-rays defined by a 5 µm pinhole located 25 mm upstream. The incident intensity of 4×10^6 photons s^{-1} μm^{-2} is high enough to cause rapid structural changes to the cell (discussed in the next section), so the sample requires pre-irradiation for about 30 minutes prior to collection of the final data set intended for reconstruction. The

final data set, shown in Fig. 9.3.3.1, is a 1024 × 1024 pixel subset of the full CCD and extends to a resolution of 11 nm at the edge and 7.8 nm in the corner. Speckles extend to the corner of the data set after a total exposure of 406 s and to the edge after 226 s.

The full reconstruction of this type of data set can only proceed once a high-fidelity support is determined. Algorithmic support determination using *Shrinkwrap*, a variation on the hybrid input–output algorithm, is straightforward for objects with sharp boundaries, as is often the case in the material sciences (Marchesini *et al.*, 2003; Chapman *et al.*, 2006). However, biological samples which often have soft boundaries require manual intervention in the early stages of reconstruction. The soft-edge problem is exacerbated by the loss of low spatial frequency information behind the beamstop. A combination of *Shrinkwrap* support adjustments and intuitively reasonable manual adjustments are made until the algorithm is stable to automatic adjustment. This point is found when further *Shrinkwrap* adjustments no longer alter the shape of the support but just its tightness. High-fidelity reconstructions of complex-valued objects are not possible with a loose support (Fienup, 1987). Once the support is found, the final image is produced as the average over many reconstructions, all using the same support, which are started from different random phase sets. This averaging procedure, discussed earlier, reduces features that are primarily due to noise and provides a measure of the reproducibility of the recovered phases and therefore an estimate of the resolution. The final reconstruction shown in Fig. 9.3.3.1 had PRTF values above 0.5 for spatial frequencies extending to the edge of the data set or 11 nm resolution. The inset image clearly shows features of the order of 15 nm in size. In general, it is not possible to identify cell organelles without labelling specific proteins. However, a correlative study of yeast which combines high-resolution CXDM with optical fluorescence would be a powerful tool for the cell-biology community. This technique has already been demonstrated at lower resolutions using a transmission X-ray microscope (Le Gros *et al.*, 2009).

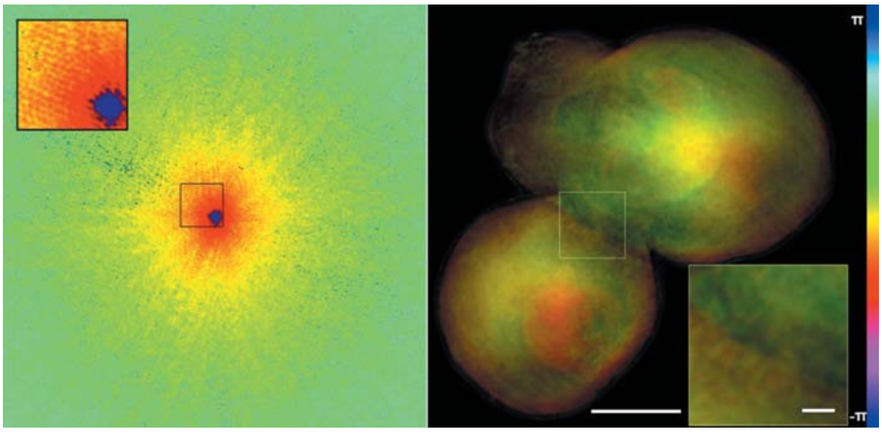

Figure 9.3.3.1
Diffraction pattern (left) and reconstruction (right) of a freeze-dried budding yeast cell. The diffraction pattern, measured on Beamline 9.0.1 of the ALS, extends to a half-period resolution of 11 nm and required 226 s of X-ray exposure. The blue regions of the diffraction pattern represent zeroes (noisy measurements or pixels lost behind the beamstop) and were left unconstrained during phase retrieval. The image represents the complex-valued X-ray wavefield after passing completely through the scattering potential, but propagated to the interior plane with the smallest support. The X-ray phase is represented as image hue and magnitude as brightness. The PRTF (not shown) never dips below 0.5, indicating that the magnitudes were adequately phased to the corner of the recorded data. The large scale bar is 1 μm, while the inset scale bar is 100 nm. The reconstruction presented here is the average of 25 independent reconstructions, each starting with a different set of random phases. Each reconstruction required 2000 iterations of the hybrid input–output algorithm and took about 14 s to complete on an nVidia Tesla C1060 graphics processing unit.

9.3.3.1. Radiation damage

High-resolution imaging of single particles with X-rays requires a large radiation dose because of the very strong dependence of the scattering cross section on spatial frequency and because, in the single-particle case, there is none of the coherent amplification one obtains when many identical copies of the particle are arranged into a crystal. This large dose means that either the sample must be protected from morphological changes induced by radiation exposure, most effectively through cryogenic techniques, or that the obtained images will represent an altered form of the original sample. Cryoprotection of hydrated cells has been successfully used in electron microscopy and lens-based X-ray microscopy for some time, but the sample preparation requirements of diffractive imaging are more severe, so the development of cryotechniques has been slower. The requirements of a finite sample support and that the sample be maintained on a zero-scattering background are extraordinarily difficult to achieve when that background consists of a micron-thick layer of ice. This is an active area of research by several X-ray diffraction microscopy groups.

For the case of dry cells, various preparation techniques (freeze drying or chemical fixation and dehydration) can preserve the large-scale internal structure, such as the size and shape of large organelles, but the ultrastructure will inevitably show artifacts of the drying process. Furthermore, exposure to ionizing radiation results in the well known shrinkage problem. Studies with a transmission X-ray microscope indicate that X-ray induced shrinkage primarily produces a higher-density but smaller version of the original cell (Jearanaikoon & Abraham-Peskir, 2005). The effect of cell shrinkage on the X-ray diffraction pattern is shown in Fig. 9.3.3.2. A freeze-dried cell is repeatedly exposed to 750 eV X-rays from Beamline 9.0.1 of the ALS. Each exposure is 30 s and delivers an X-ray dose of approximately 5×10^8 Gy. The sample is stable for the first two exposures but then experiences a rapid collapse, followed by a slow but continuous shrinkage. The collapse is apparent from the elongated speckles, which indicate a sample for which the diameter is changing during the exposure while its relative structure is maintained. Overall, the sample loses about 25% of its volume prior to the final exposure used for reconstruction (Shapiro *et al.*, 2005; Thibault *et al.*, 2006). Over the course of this exposure series the total scattered signal does not change, indicating that the total mass of the sample remains intact. The rapid change in the diffraction pattern during the early exposures means that successful imaging experiments require pre-irradiation of the sample. The slow but continuous shrinkage of dry samples with further dose means that the resolution of the three-dimensional images will necessarily be reduced. Indeed, Nishino *et al.* (2009) observed reduced resolution in their three-dimensional reconstruction of a dry

chromosome because of morphological changes which occurred during data collection. Hence, full three-dimensional imaging of cells by diffractive methods requires cryogenic protection against radiation damage. Predictions based on a calculation of the cross section for coherent scattering by a smooth dielectric indicate that 10 nm resolution imaging of frozen hydrated organic matter should be possible using soft X-rays at currently available synchrotron sources (Howells *et al.*, 2009). This limit is arrived at through a comparison of the radiation dose required for imaging and the dose at which radiation damage has been empirically observed at different length scales. However, it seems plausible that the presence of many identical particles within a cell could be exploited to provide super-resolution information.

9.3.3.2. Low-dose three-dimensional imaging; low damage potential of stereoscopic viewing

Diffraction imaging in three dimensions proceeds as it does in standard X-ray tomography. That is, two-dimensional data are recorded from many angular orientations of the sample and then assembled into a three-dimensional data set. In this case, however, the data are recorded in reciprocal space and the individual data sets only need to be registered with respect to the angular coordinate due to the Fourier shift theorem. In the absence of any additional information, the angular sampling of reciprocal space is determined by the Crowther resolution,

$$k_C = \frac{1}{\Delta\theta D},$$

where D is the object diameter and $\Delta\theta$ is the angular separation of the two-dimensional data sets. This is the spatial frequency at which the unmeasured Fourier components, those in between the measured Ewald sphere segments, can be properly interpolated from the measured data. Diffraction microscopy, however, requires the addition of information in the form of real-space constraints. This additional information allows for the calculation of not only the missing reciprocal-space phases but also a limited number of missing magnitudes. Chapman *et al.* (2006) showed that $\Delta\theta$ could in fact be up to four times larger than required by the Crowther relation, with k_C matching the numerical aperture of the imaging system. Thus, three-dimensional reconstructions could take place with nearly isotropic diffraction-limited resolution with only about 150 angular orientations of the sample.

Stereoscopic viewing can provide a significant degree of three-dimensional perception of an extended object while only increasing the total radiation exposure by a factor of two. In principle, according to the dose-fractionation theorem of Hegerl and Hoppe, full three-dimensional visualization of a given resolution element should not require a dose any higher than two-dimensional visualization of the same element with the same statistical accuracy (Hegerl & Hoppe, 1976). This theorem provides hope that high-resolution imaging in three-dimensions, perhaps even of dry specimens, is possible, but in practice this is very difficult to achieve and low-dose imaging techniques are only now being explored by the CXDM community. Stereoscopic viewing should be considered the preliminary low-dose technique of choice. One particular advantage is the rapid reconstruction (compared with full three-dimensional reconstructions) which makes possible *in situ* sample inspection. Fig. 9.3.3.3 shows a stereo image of a chemically dried budding yeast cell. When viewed stereoscopically, with the viewer's focus in front of the image, the three-dimensional arrangement of a group of vesicles in the mother cell can be visualized.

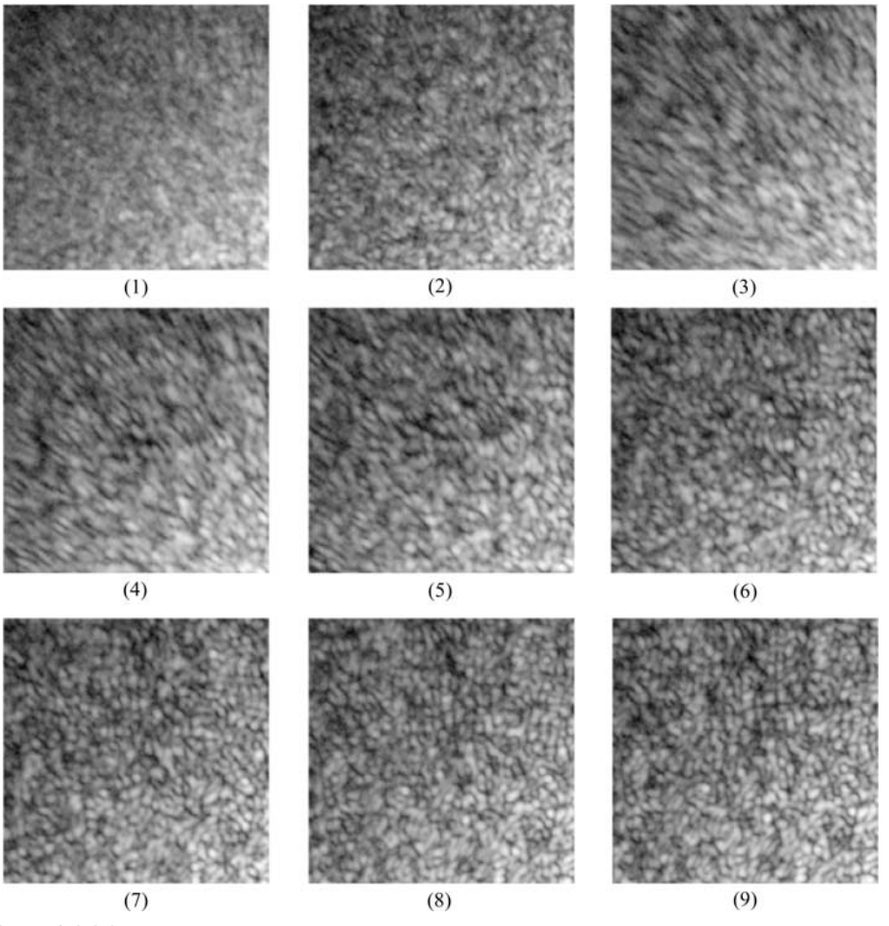

Figure 9.3.3.2
Exposure to ionizing radiation causes shrinkage of organic matter. Each image in this series is a section of a measured diffraction pattern from a freeze-dried yeast cell. The images were taken sequentially and each represents an additional X-ray dose of 5×10^8 Gy. After a cumulative dose of 1×10^9 Gy, the cell undergoes a rapid collapse [apparent from the elongated speckles in images (3)–(5)] followed by continued shrinkage at a reduced rate. The X-rays used had an energy of 750 eV and a dose of 5×10^8 Gy was adequate for reconstruction at 30 nm resolution. (Reproduced from Shapiro, 2004).

9.3.4. Conclusions

CXDM promises to be a highly efficient imaging methodology which can deliver high-resolution and high-contrast images of large non-crystalline biological structures. Radiation-induced shrinkage of dry cells will probably prohibit three-dimensional imaging of such cells at high resolution. However, significant three-dimensionality can be achieved through stereoscopic viewing of a cell, which only doubles the necessary X-ray dose. Even so, in the absence of low-dose diffraction techniques the sample must undergo considerable morphological change prior

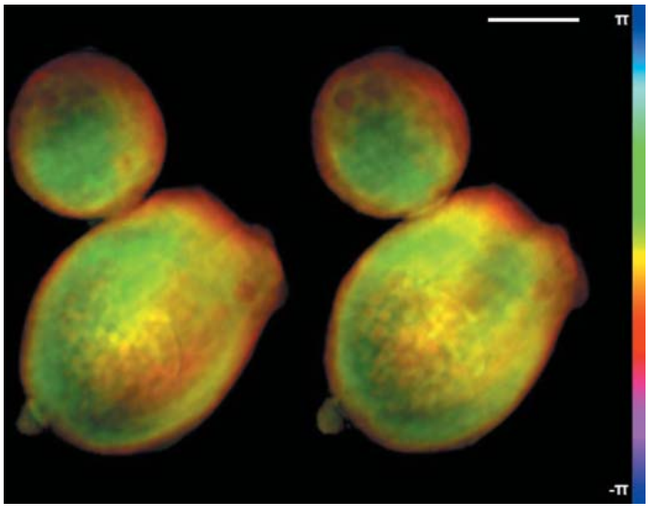

Figure 9.3.3.3
Stereo image of a budding yeast cell. This budding yeast cell was chemically fixed with gluteraldehyde and dehydrated in acetone. The images have an angular separation of 10° and a pixel size of 11 nm. The three-dimensional arrangement of a group of small vesicles in the mother cell can be visualized when viewed stereoscopically (with the viewer's focus in front of the image). The scale bar is 500 nm.

to imaging, although this change does not seem to alter the relative arrangement of organelles. The development of low-dose techniques will allow for the direct observation of these radiation-induced changes. In the long run, it is cryogenic protection that provides the most valuable structural information, since the cells are maintained in a near living state. Ultra-high-resolution three-dimensional imaging will still require the development of low-dose techniques, as cryoprotected samples have also been observed to suffer from mass loss with the accumulation of very high X-ray doses ($>10^{10}$ Gy). These imaging techniques are currently under development at the ALS in collaboration with Stony Brook University and elsewhere. Alternatively, X-ray free-electron lasers (FELs) promise the highest resolution imaging of living cells that is possible by any means; indeed, it has been proposed that sub-nanometre resolution is possible (Bergh *et al.*, 2008). The ultra-short and ultra-bright pulses of an X-ray FEL will encode the structural information from a living cell before it is destroyed by the pulse.

The author would like to thank Johanna Nelson and Xiaojing Huang of Stony Brook University for preparing the samples and providing the diffraction data for reconstruction. This work was supported under the Seaborg Fellowship at Lawrence Berkeley National Laboratory and by grants from the National Institutes of Health, the National Science Foundation and the US Department of Energy to Stony Brook University. The Advanced Light Source at Lawrence Berkeley National Laboratory is supported by the Director, Office of Science, Office of Basic Energy Sciences, Materials Sciences Division, of the US Department of Energy.

References

Barty, A., Marchesini, S., Chapman, H. N., Cui, C., Howells, M. R., Shapiro, D. A., Minor, A. M., Spence, J. C., Weierstall, U., Ilavsky, J., Noy, A., Hau-Riege, S. P., Artyukhin, A. B., Baumann, T., Willey, T., Stolken, J., van Buuren, T. & Kinney, J. H. (2008). *Three-dimensional coherent X-ray diffraction imaging of a ceramic nanofoam: determination of structural deformation mechanisms. Phys. Rev. Lett.* **101**, 055501.

Bates, R. H. T. (1982). *Fourier phase problems are uniquely soluble in more than one dimension. I. Underlying theory. Optik (Stuttgart)*, **61**, 247–262.

Bates, R. H. T. & Fright, W. R. (1983). *Composite two-dimensional phase-restoration procedure. J. Opt. Soc. Am.* **73**, 358–365.

Bergh, M., Huldt, G., Timneanu, N., Maia, F. R. & Hajdu, J. (2008). *Feasibility of imaging living cells at subnanometer resolutions by ultrafast X-ray diffraction. Q. Rev. Biophys.* **41**, 181–204.

Chao, W., Kim, J., Rekawa, S., Fischer, P. & Anderson, E. H. (2009). *Demonstration of 12 nm resolution Fresnel zone plate lens based soft X-ray microscopy. Opt. Express*, **17**, 17669–17677.

Chapman, H. N., Barty, A., Marchesini, S., Noy, A., Hau-Riege, S. P., Cui, C., Howells, M. R., Rosen, R., He, H., Spence, J. C., Weierstall, U., Beetz, T., Jacobsen, C. & Shapiro, D. (2006). *High-resolution ab initio three-dimensional X-ray diffraction microscopy. J. Opt. Soc. Am. A Opt. Image Sci. Vis.* **23**, 1179–1200.

Fienup, J. R. (1978). *Reconstruction of an object from the modulus of its Fourier transform. Opt. Lett.* **3**, 27–29.

Fienup, J. R. (1982). *Phase retrieval algorithms: a comparison. Appl. Opt.* **21**, 2758–2769.

Fienup, J. R. (1987). *Reconstruction of a complex-valued object from the modulus of its Fourier transform using a support constraint. J. Opt. Soc. Am. A Opt. Image Sci. Vis.* **4**, 118–123.

Fienup, J. R., Crimmins, T. R. & Holsztynski, W. (1982). *Reconstruction of the support of an object from the support of its autocorrelation. J. Opt. Soc. Am.* **72**, 610–624.

Gerchberg, R. W. & Saxton, W. O. (1972). *A practical algorithm for the determination of phase from image and diffraction plane pictures. Optik (Stuttgart)*, **35**, 237–246.

Hegerl, R. & Hoppe, W. (1976). *Influence of electron noise on three-dimensional image reconstruction. Z. Naturforsch. Teil A*, **31**, 1717–1721.

Howells, M. R., Beetz, T., Chapman, H. N., Cui, C., Holton, J. M., Jacobsen, C. J., Kirz, J., Lima, E., Marchesini, S., Miao, H., Sayre, D., Shapiro, D. A., Spence, J. C. H. & Starodub, D. (2009). *An assessment of the resolution limitation due to radiation damage in X-ray diffraction microscopy. J. Electron Spectrosc. Relat. Phenom.* **170**, 4–12.

Huang, X., Nelson, J., Kirz, J., Lima, E., Marchesini, S., Miao, H., Nieman, A. M., Shapiro, D., Steinbrener, J., Stewart, A., Turner, J. J. & Jacobsen, C. (2009). *Soft X-ray diffraction microscopy of a frozen hydrated yeast cell. Phys. Rev. Lett.* **103**, 198101.

Jearanaikoon, S. & Abraham-Peskir, J. V. (2005). *An X-ray microscopy perspective on the effect of glutaraldehyde fixation on cells. J. Microsc.* **218**, 185–192.

Larabell, C. A. & Le Gros, M. A. (2004). *X-ray tomography generates 3-d reconstructions of the yeast, Saccharomyces cerevisiae, at 60 nm resolution. Mol. Biol. Cell*, **15**, 957–962.

Le Gros, M. A., McDermott, G., Uchida, M., Knoechel, C. G. & Larabell, C. A. (2009). *High-aperture cryogenic light microscopy. J. Microsc.* **235**, 1–8.

Lima, E., Wiegart, L., Pernot, P., Howells, M. R., Timmins, J., Zontone, F. & Madsen, A. (2009). *Cryogenic X-ray diffraction microscopy for biological samples. Phys. Rev. Lett.* **103**, 198102.

Marchesini, S. (2007). *A unified evaluation of iterative projection algorithms for phase retrieval. Rev. Sci. Instrum.* **78**, 011301.

Marchesini, S., He, H., Chapman, H. N., Hau-Riege, S. P., Noy, A., Howells, M. R., Weierstall, U. & Spence, J. C. H. (2003). *X-ray image reconstruction from a diffraction pattern alone. Phys. Rev. B*, **68**, 140101.

Miao, J., Charalambous, P., Kirz, J. & Sayre, D. (1999). *Extending the methodology of X-ray crystallography to allow imaging of micrometre-sized non-crystalline specimens. Nature (London)*, **400**, 342–344.

Miao, J., Ishikawa, T., Johnson, B., Anderson, E. H., Lai, B. & Hodgson, K. O. (2002). *High resolution 3D X-ray diffraction microscopy. Phys. Rev. Lett.* **89**, 088303.

Miao, J., Sayre, D. & Chapman, H. N. (1998). *Phase retrieval from the magnitude of the Fourier transforms of nonperiodic objects. J. Opt. Soc. Am. A Opt. Image Sci. Vis.* **15**, 1662–1669.

Nelson, J., Huang, X., Steinbrener, J., Shapiro, D. A., Kirz, J., Marchesini, S., Neiman, A. M., Turner, J. & Jacobsen, C. (2010). *High resolution X-ray diffraction microscopy of specifically labelled yeast cells. Proc. Natl Acad. Sci. USA*, **107**, 7235–7239.

Nishino, Y., Takahashi, Y., Imamoto, N., Ishikawa, T. & Maeshima, K. (2009). *Three-dimensional visualization of a human chromosome using coherent X-ray diffraction. Phys. Rev. Lett.* **102**, 018101.

Pfeifer, M. A., Williams, G. J., Vartanyants, I. A., Harder, R. & Robinson, I. K. (2006). *Three-dimensional mapping of a deformation field inside a nanocrystal. Nature (London)*, **442**, 63–66.

Sayre, D. (1980). *Imaging Processes and Coherence in Physics*, edited by M. Schlenker, M. Fink, J. P. Goedgebuer, C. Malgrange, J. Ch. Viénot & R. H. Wade, p. 229. Heidelberg: Springer-Verlag.

Sayre, D. (1991). *Direct Methods of Solving Crystal Structures*, edited by H. Schenk, pp. 353–355. New York: Plenum Press.

Sayre, D. (2008). *Report on a project on three-dimensional imaging of the biological cell by single-particle X-ray diffraction. Acta Cryst.* A**64**, 33–35.

Sayre, D. & Chapman, H. N. (1995). *X-ray microscopy. Acta Cryst.* A**51**, 237–252.

Schroer, C. G., Boye, P., Feldkamp, J. M., Patommel, J., Schropp, A., Schwab, A., Stephan, S., Burghammer, M., Schöder, S. & Riekel, C. (2008). *Coherent X-ray diffraction imaging with nanofocused illumination. Phys. Rev. Lett.* **101**, 090801.

Shapiro, D., Thibault, P., Beetz, T., Elser, V., Howells, M., Jacobsen, C., Kirz, J., Lima, E., Miao, H., Neiman, A. M. & Sayre, D. (2005). *Biological imaging by soft X-ray diffraction microscopy. Proc. Natl Acad. Sci. USA*, **102**, 15343–15346.

Shapiro, D. A. (2004). *Biological Imaging by Soft X-ray Diffraction Microscopy*. PhD thesis, Stony Brook University.

Thibault, P., Elser, V., Jacobsen, C., Shapiro, D. & Sayre, D. (2006). *Reconstruction of a yeast cell from X-ray diffraction data. Acta Cryst.* A**62**, 248–261.

Wang, Y., Jacobsen, C., Maser, J. & Osanna, A. (2000). *Soft X-ray microscopy with a cryo scanning transmission X-ray microscope: II. Tomography. J. Microsc.* **197**, 80–93.

Weiss, D., Schneider, G., Niemann, B., Guttman, P., Rudolph, D. & Schmahl, G. (2000). *Computed tomography of cryogenic biological specimens based on X-ray microscopic images. Ultramicroscopy*, **84**, 185–197.